JACS
JOURNAL OF THE AMERICAN CHEMICAL SOCIETY

ARTICLE

pubs.acs.org/JACS

Switching on the Electrocatalytic Ethene Epoxidation on Nanocrystalline RuO_2

Jakub S. Jirkovský,*[,†,‡] Michael Busch,[‡] Elisabet Ahlberg,[‡] Itai Panas,[§] and Petr Krtil[†]

[†]J. Heyrovsky Institute of Physical Chemistry, Dolejškova 3, Prague, Czech Republic

[‡]Department of Chemistry, University of Gothenburg, Kemigården 4, S-412 96 Gothenburg, Sweden

[§]Department of Chemistry and Biotechnology, Chalmers University of Technology, S-412 96 Gothenburg, Sweden

Supporting Information

ABSTRACT: Ruthenium-based oxides with rutile structure were examined regarding their properties in electrocatalytic ethene oxidation in acid media. A possible promoting effect of chloride ions toward oxirane formation was explored. Online differential electrochemical mass spectrometry combined with electrochemical polarization techniques were used to monitor the potential dependence of organic products resulting from ethene oxidation as well as the reaction solution decomposition products. Quantum chemical modeling by means of density functional theory was employed to study key reaction steps. The ethene oxidation in acid media led to CO_2, whereas oxirane was formed in the presence of 0.3 M Cl^-. In the Cl^- promoted oxidation on RuO_2, oxirane and a small amount of CO_2 were the only detected electro-oxidation products at potentials below the onset of Cl_2 and O_2 evolution, resulting from Cl^- and water oxidation. It is demonstrated here that the epoxidation is a surface-related electrocatalytic process that depends on the surface properties. Cl acts as the epoxidation promoter that switches off the combustion pathway toward CO_2 and enables the epoxidation reaction channel by surface reactive sites blocking. The proposed epoxidation mechanism implies binuclear (recombination) mechanism for O_2 evolution reaction on considered surfaces.

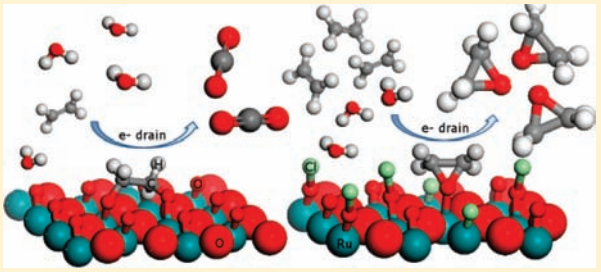

INTRODUCTION

Epoxidation reactions represent a high added value for transformation of olefins.[1] As such, the technology of olefin epoxide production is an area with great development potential. For instance, new large scale manufacture of propylene oxide, where H_2O_2 is used to oxidize propylene on titanium silicate TS-1, has been launched recently.[2−4] One of the alternative routes toward an epoxide formation comprises an electrochemical oxidation of alkenes. A possible implementation of the electrochemical approach would provide a more energy efficient way of synthesis by cogeneration of electric energy and valuable chemicals.[5,6]

The electrochemical oxidation of olefins has been examined since 1960s. In the early studies of ethene oxidation on various metals, carbon dioxide was found as the main product on Pt, Ir, and Rh.[7] Aldehydes were predominant on Au and Pd.[7−9] Later, chromatography and in situ mass spectrometry confirmed acetaldehyde and small amount of CO_2 as the reaction products on Au.[10,11] The interactions of ethene with Au and Pt electrode surfaces have been investigated by spectroscopic[12,13] as well as quantum chemical methods in the case of Au.[11] It was concluded that ethene adsorbs parallel to the surface utilizing the π orbitals of ethene in the surface chemical bond.[10−13] By density functional theory (DFT) on Au as well as on Ag, two intermediate structures of ethene were identified on the surface, where one determines CO_2 as the final product and the second leads to oxirane.[11,14] Importantly, the effects of static electric field, due to electrode polarization, and the addition of solvent environment were found to have a minor influence on the calculated results on Au.[11]

In contrast to electrocatalytic processes confined to liquid electrolytes, the epoxidation reactions do not represent a major challenge in the gas phase heterogeneous catalysis. Today, industrial gas phase conversion of ethene to oxirane commonly employs silver as the catalyst.[14−16] Cs and Cl are successfully used as catalytic promoters to increase the Ag catalyst selectivity toward oxirane, from about 50% to 80%.[16] It has been proposed that Cs co-adsorbs on the Ag surface and stabilizes the reaction intermediate by electric field/dipole interactions. This effect promotes oxirane formation and suppresses the combustion route.[16] The detailed role of Cl in the reaction process is not yet clear, although atomic Cl has been proposed to diffuse into the Ag catalyst, thus causing subsurface enhancement of the Cs effect.[16]

One of the electrochemical approaches toward epoxide production is the electro-oxidation of alkenes in alkaline media in a presence of halogenide ions.[8,17−19] It is commonly referred to as

Received: November 5, 2010
Published: March 25, 2011

the "indirect route". It is suggested that the process proceeds via halohydrin route where, e.g., 2-chloroethanol is formed by oxidation of ethene with unspecified electrochemically formed chloro-species near the electrode surface.[8] 2-Chloroethanol subsequently undergoes homogeneous base-promoted dehydrogenhalogenation to form the oxirane.[17] As a result, the indirect epoxidation in alkaline electrolytes gives high yields of epoxides and the electro-oxidation in acidic solutions leads to accumulation of halohydrins.[17−19] The evidence to support the proposed reaction mechanisms presented in the latter papers, however, is rather inconclusive. In particular, the role of the halide ions in the electrochemical oxidation of alkenes remains unclear.

The present effort explores the possibility of electrocatalytic oxidation of ethene to produce oxirane in acid media, most compatible with fuel cell technology.[20] The role of Cl^- in the reaction process is evaluated. It is suggested here that Cl^- may display a dual function as catalytic epoxidation promoter and reactant to form Cl_2 and 2-chloroetanol. The aim is to investigate to what extent the two functions of Cl^- can be decoupled by choice of catalyst, thus isolating a promoting effect of Cl^-. RuO_2 has been long known as an active and stable electrode material for water and Cl^- oxidation in acid media.[21] In addition, these electrocatalytic properties of the Ru based oxides can be tuned by controlling the particle size[22] or by doping with, e.g., Ni[23] or Co.[24] In the present paper, the efficiency of an analogous electrocatalysts, i.e., nanocrystalline RuO_2 and Co doped RuO_2, toward ethene oxidation in acid media is investigated by online mass spectrometry. To clarify the role of chloride ions in the reaction mechanisms, DFT calculations are employed. The comparison between results of theory and experiment is discussed.

METHODS

Chemicals. Cobalt(II) nitrate (ACS grade), 30% H_2O_2 solution (semiconductor grade), acetaldehyde (ACS grade), 70% redistlilled $HClO_4$ (99.999%), and NaCl (p.a.) were purchased from Sigma-Aldrich. Ruthenium(III) nitrosylnitrate and 25% tetramethylammonium hydroxide (electronic grade) were supplied by Alpha Aesar. Titanium mesh (20% open area) was from Goodfellow (U.K.). Ethene (98%) gas was obtained from Linde Gas (Czech Republic). Milli-Q (Millipore Inc.) water was used in all experiments.

Materials Preparation. The RuO_2[22,25] and the $Ru_{0.8}Co_{0.2}O_2$[24,26] samples were prepared using a sol−gel approach described previously. Starting solutions of either ruthenium(III) nitrosylnitrate or of ruthenium(III) nitrosylnitrate with cobalt(II) nitrate in a mixture of ethanol and propane-2-ol (1:1) were precipitated with aqueous solution of tetramethylammonium hydroxide. In the case of starting solution containing both Ru and Co the actual Ru/Co ratio was 4:1. Both precipitation procedures led to a formation of amorphous precursors that were filtered and annealed. The RuO_2 precursor was treated with H_2O_2 prior to the annealing. The precursor containing both Ru and Co was aged in a PTFE lined stainless steel autoclave at 100 °C for 40 h to facilitate the filtration process. The RuO_2 precursor was annealed at 400 °C (RuO_2-400) and 900 °C (RuO_2-900) and the $Ru_{0.8}Co_{0.2}O_2$ precursor at 800 °C in air for 4 h.

Materials Characterization. The crystallinity and phase purity of the prepared samples were checked using Bruker D8 Advance powder X-ray diffractometer with Vantec-1 detector and CuK_α radiation source. The X-ray diffraction analysis confirmed that all materials were of a single-phase character with rutile type structure ($P4_2/mnm$).[22,26] Both RuO_2-400 and RuO_2-900 materials showed good particle size monodispersity with mean diameters of 15 ± 9 and 35 ± 9 nm, respectively.[22] The particle shape analysis showed predominance of 101 (∼55%) and 110 (∼35%) oriented planes for both materials.[22] The Co surface concentration in $Ru_{0.8}Co_{0.2}O_2$ determined by XPS was higher compared to bulk and was around ∼30%.[24] The analysis of particle shape and size distribution of $Ru_{0.8}Co_{0.2}O_2$ showed similar results as RuO_2; the mean diameter was 56 ± 14 nm and (101) was also the predominant surface orientation followed by (110).[24]

Electrodes. The electrodes for electrochemical experiments were prepared from RuO_2-400, RuO_2-900, and $Ru_{0.8}Co_{0.2}O_2$ materials by sedimentation of nanocrystalline powder from a water-based suspension on Ti mesh. The duration of the deposition was adjusted to obtain the surface coverage of about 1−2 mg/cm^2 of active oxide layer. The deposited layers were stabilized by annealing the electrodes for 20 min at 400 °C in air. The initial oxide suspensions were prepared in an ultrasound bath and contained approximately 5 g/L of ruthenium-based oxide in water.

Elecrochemical Setup. The electrochemical behavior of the prepared materials was studied by cyclic voltammetry combined with differential electrochemical mass spectrometry (DEMS). All experiments were performed in a homemade Kel-F single compartment cell[27] in a three electrode arrangement controlled by a PAR 263A potentiostat. Pt and saturated calomel electrode (SCE) were used as an auxiliary and a reference electrode, respectively. For clarity, measured potentials were recalculated and all reported data in the paper are referenced versus the normal hydrogen electrode (NHE; +0.244 V vs SCE). The measurements were carried out in 0.1 M $HClO_4$ aqueous solution, both ethene-free and saturated with ethene. The effect of chloride ions was studied in 0.1 M $HClO_4$ containing 0.001, 0.01, and 0.3 M NaCl, respectively. The potential sweep rate was 15 mV s^{-1} in all experiments, which provided optimal compromise between obtaining near steady state behavior and reasonable measurement times with respect to the lifetime of the mass detector. The cell was sealed against the ambient atmosphere, and saturation of the solution with ethene (5.2 mM) was maintained by ethene circulation loop at the ambient pressure and temperature (25 °C). The electrochemical compartment was separated from the mass spectrometer vacuum inlet by PTFE membrane (Gore, 100 nm pore size). The investigated electrode was pressed against the membrane allowing immediate detection of any volatile products formed at the electrode.

DEMS. The DEMS apparatus consisted of Prisma TM QMS200 quadrupole mass spectrometer (Balzers) connected to TSU071E turbomolecular drag pumping station (Balzers). The mass spectrometer was set up to monitor all mass to charge ratio (m/z) channels that could be expected from fragmentation of likely products of ethene oxidation. Ethylene glycol, acetic acid, acetaldehyde, oxirane, and 2-chloroethanol were considered. Fragmentation patterns for all monitored species were obtained from online NIST spectral library[28] and adjusted for the employed spectrometer. The calibration of the mass detector was carried out by measuring its response after injection of acetaldehyde and ethene to the electrochemical cell attached to the mass spectrometer. In the same way injected ethylene glycol did not penetrate the PTFE membrane and cannot be detected by the employed equipment. The fragmentation patterns for the rest of considered species were corrected according to the calibration assuming the same trend of the detector sensitivity increase toward fragments with lower mass as for ethene and acetaldehyde. The calibrated fragmentation patterns of all monitored species are summarized in Table 1.

Computational Details. The initial crystal structure was of rutile type ($P4_2/mnm$) with lattice parameters $a = b = 4.559$ Å and $c = 3.166$ Å as resulted from geometry optimization (DMOL3[29]). Oxygen terminated two-layer as well as three-layer slabs with (101) crystallographic orientation were obtained by cleavage of the initial structure and were of the size of 2 × 2 unit cell, with respect to the surface plane (see Figure S1 in Supporting Information). In both cases, the bottom layers were frozen

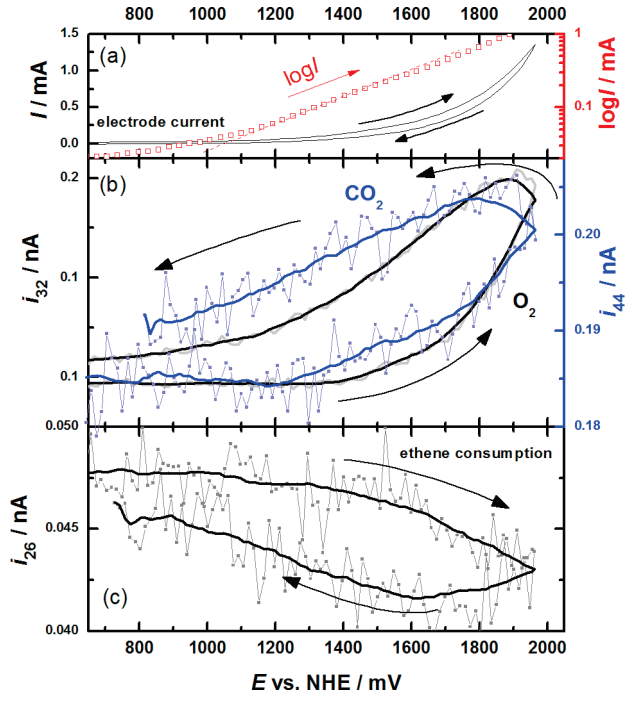

Figure 1. Ethene oxidation on the RuO_2-900 electrode in 0.1 M $HClO_4$. (a) Current response during electrode polarization (left *y* axis) and logarithmic dependence of the same current highlighted in red (squares; right *y* axis). Simultaneously recorded DEMS signals $i_{m/z}$ for (b) m/z of 44 (blue; right *y* axis), 32 (black; left *y* axis), and (c) 26 in relationship with potential. The thick lines are added to guide the eye and were obtained by smoothing of the measured i_{44} and i_{26} data (adjacent averaging, 15 points). Sweep rate = 15 mV s^{-1}.

in the crystal structure configuration, i.e., only the top layer was allowed to relax after the introduction of the interface and the surface chemistry. In the case of the two layer slab the generalized gradient approximation (GGA) PBE density functional[30] as implemented in the DMOL3 program package was employed in conjunction with the double-ξ numerical basis set with polarization functions (DNP) and hardness conserving semilocal pseudopotentials[31] for describing the inert core electrons. The same functional but in the CASTEP[32] implementation, which spans the Kohn−Sham orbitals in a plane-wave basis, was employed for the three-layer slab calculations. In the case of the latter, core electrons were described by ultrasoft pseudopotentials[33] in conjunction with cutoff energy of 300 eV. Convergence criteria for the SCF part were 3×10^{-5} eV (4×10^{-7} eV) and for the geometry optimization were 3×10^{-4} eV/atom (2×10^{-6} eV/atom) for DMOL3 (CASTEP) calculations. Both program packages were accessed from the Material Studios program suite framework.[34] Results from Γ-point calculations are reported throughout. Similar approach has been applied successfully for description of RuO_2.[35] The consistency of computational results obtained for propylene epoxidation on titanium silicate catalyst has shown the applicability of DFT in these type of reactions.[36] The effects of solvent and static electric field on the epoxidation reactions, not taken into account in the present paper, are discussed in references 37 and 11, respectively.

RESULTS AND DISCUSSION

Electrode Materials. The electrocatalytic materials examined in this study were selected to reflect the role of the Cl^- in the ethene oxidation. The considered electrocatalysts show significant variability in the selectivity toward Cl^- oxidation to Cl_2 gas,[22,24] which was ascribed either to the particle shape effects (in the case of RuO_2 materials)[22] or to local structure effects (in the case of Co doped materials).[24] The solid state characterization of the materials investigated in this work confirmed good reproducibility of employed synthetic methods,[25,26] and the details can be found in Methods. All electrode materials were of nanocrystalline (mean diameter <56 nm) and single-phase character (rutile).

Ethene Oxidation on Ru Oxides. The ethene oxidation on the RuO_2-900 electrode in 0.1 M $HClO_4$ is depicted in Figure 1. Current measured during the electrode polarization is shown in Figure 1a and the simultaneous DEMS based analysis of the volatile reaction products in Figure 1b and c. The onset of the exponential anodic current in Figure 1a triggers an increase of abundance of the mass fragments with m/z ($i_{m/z}$) of 44 (i_{44}) at ~1.2 V and 32 (i_{32}) at ~1.35 V (Figure 1b). The increase of the i_{32} signal can be ascribed to O_2 resulting from water oxidation at the electrode. The alternation of the i_{44} signal can be attributed to CO_2 or to various organic species. The measured signal on the i_{44} is not tracked by any signal attributable to organic compounds expected to form in this system. It is, therefore, reasonable to assume that CO_2 is the only product of ethene oxidation. The potential dependence of the i_{44} signal is inversely tracked by i_{26}, which is characteristic for ethene consumed at the electrode (Figure 1c). For comparative reasons, a ratio between the integral intensity attributed to ethene consumption (Δq_{26}) and CO_2 production (Δq_{44}) was calculated as illustrated in Supporting Information Figure S2. The $\Delta q_{26}/\Delta q_{44}$ ratio equals to ~0.25 for all materials considered. Similarly to RuO_2-900, no additional fragments were detected on the RuO_2-400 and $Ru_{0.8}Co_{0.2}O_2$ electrodes. Therefore, it can be concluded that there is no qualitative difference between properties of the studied materials toward ethene oxidation in 0.1 M $HClO_4$.

Cl^- Effects on RuO_2; [Cl^-] ≤ 0.01 M. The effect of Cl^- on ethene oxidation was examined on RuO_2-900 in 0.1 M $HClO_4$ solutions with gradually increasing Cl^- concentration as illustrated in Figure 2. The experiments were conducted in the same way as in Cl^- free solution (Figures 1 and 2a). The time dependence of i_{44} and i_{26} during cyclic linear potential sweep is shown here for different concentrations of Cl^-. Simultaneously recorded i_{32} (O_2) signals and electrode potential ramps are also shown in Figure 2 for each Cl^- concentration. Based on the assumption that for concentrations of Cl^- of 0.01 M or lower the O_2 evolution is not significantly affected by Cl^-, the DEMS data in Figure 2a−c were normalized with respect to the O_2 signal (i_{32}) at 1.7 V. This assumption was supported by the fact that the Cl_2 evolution was below the detection limit of the mass spectrometer. By normalization, a better comparison of the DEMS signals between different Cl^- concentrations can be provided, although it has to be borne in mind that in reality the O_2 evolution is probably suppressed due to Cl^- adsorption.[35] The original i_{44} and i_{26} DEMS data in relationship with potential obtained (1) in 0.001 and 0.01 M Cl^- containing solutions are shown in Supporting Information Figure S3 and (2) in Cl^- free solutions in Figure 1. In Figure 2a, the i_{44} signal forms a peak that is asymmetric with respect to the potential ramp. This can be due to an accumulation of formed CO_2 in the solution, which is reflected in an additional concentration-dependent CO_2 source during the negative potential sweep. The same reasoning can be applied to i_{26} and ethene resource restoration by mass transport from the bulk solution. As shown in Figure 2b and Supporting Information Figure S2b, i_{44} does not track the exponential increase during the positive potential sweep, in contrast to Cl^-

dx.doi.org/10.1021/ja109955w |*J. Am. Chem. Soc.* 2011, 133, 5882–5892

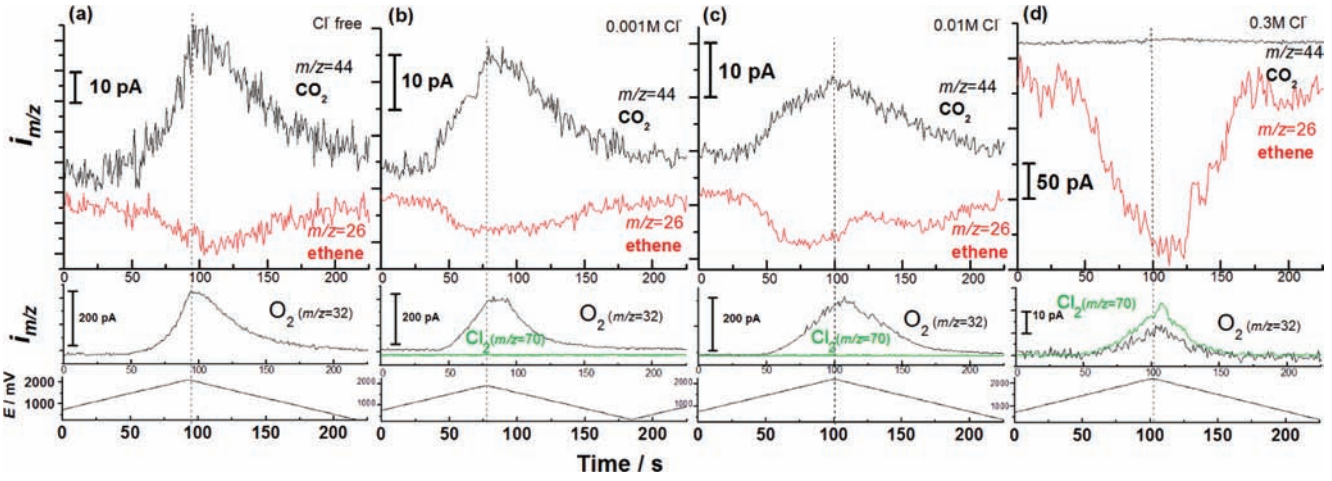

Figure 2. Mass spectrometer response $i_{m/z}$ for m/z of 44 (CO_2) and 26 (ethene) as a function of time recorded during polarization of the RuO_2-900 electrode in 0.1 M $HClO_4$ containing (a) 0, (b) 0.001, (c) 0.01, and (c) 0.3 M NaCl. Simultaneously recorded i_{32} (O_2) and i_{70} (Cl_2) signals are shown in the middle and polarization ramps applied throughout at the bottom part of each figure. The data in panels a−c were normalized with respect to the i_{32} signal at 1.7 V. The vertical lines are added to guide the eye. Sweep rate = 15 mV s^{-1}.

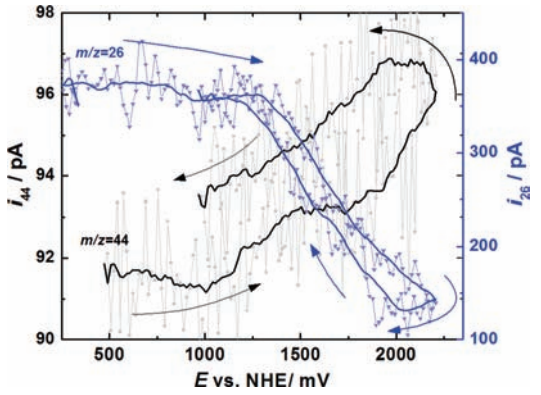

Figure 3. Mass spectrometer signals $i_{m/z}$ for m/z of 44 and 26 recorded in 0.1 M $HClO_4$, 0.3 M NaCl on RuO_2-900 electrode during electrode polarization. The thick lines obtained by smoothing (adjacent averaging, 15 points) are shown to guide the eye. Sweep rate = 15 mV s^{-1}.

free electrolyte (Figure 2a), and a hump appears around 1.7 V in 0.001 M Cl^- (Figure 2b and Supporting Information Figure S3a). A similar trend is observed in the i_{26} signal where the ethene consumption increase is interrupted at 1.7 V and a plateau appears. The observed behavior gets more complex in 0.01 M Cl^- where the i_{44} signal peak appears to divide into two or even three modes (Figure 2c and Supporting Information Figure S3b). The ethene consumption peak observed during the sweep to more positive potentials appears also during the reversed sweep and there is clear suppression of ethene consumption at high potentials. The already mentioned asymmetry of both i_{44} and i_{26} peaks with respect to the potential ramp changes with the increase of Cl^- concentration. Both signals seem to display lower values during the sweep back to lower potentials due to Cl^-. This may point on a decrease in electrode electrocatalytic activity toward ethene consumption with time during the potential sweep (see Figure 2b and c). In an additional potential sweep cycle (after reaching lower potentials first, E < 1.2 V), however, the original electrocatalytic activity seems to be restored (not shown). This may indicate a poisoning of the electrode surface by some oxidation products that are removed at low potentials

Table 1. Relative Abundance of Fragments of Monitored Species[a]

m/z	ethene	oxirane	acetaldehyde	acetic acid	2-chloroethanol
15	0.01	0.88	0.50	0	0
26	0.9	0	0.05	0	0
27	1	0	0.04	0	0
29	0.015	1	1	0	0
31	0	0	0	0	1
43	0	0.16	0.51	0.8	0.06
45	0	0.02	0.02	1	0
44	0	0.70	0.87	0.02	0.03

[a] Only fragments with m/z monitored during the measurements are shown. The most abundant fragment for a compound has an intensity of 1 (among those considered). The relative abundances were calibrated for the employed spectrometer as described in Methods.

(E < 1.2 V). Unlike in the Cl^- free solutions, the i_{26} signal does not follow the course of the i_{44} signal in detail in the presence of Cl^-, which may point to some additional process taking place at the electrode. The ethene consumption and hence the corresponding charge difference Δq_{26} remains approximately constant for Cl^- concentration up to 0.01 M. The value of the $\Delta q_{26}/\Delta q_{44}$ ratio, however, shifts from 0.25 for Cl^- free solutions to 0.33 and 0.67 for 0.001 and 0.01 M Cl^- concentration, respectively. This can only be explained by the existence of a competitive ethene oxidation channel parallel to that leading to CO_2. As no increase of abundance of any additional fragments was observed (see Supporting Information Figure 3c), we can only speculate about an alternative ethene fate. It is important to note that the detection sensitivity toward, e.g., oxirane or 2-chloroethanol, is much lower than for CO_2 because of differences in volatility, and ethylene glycol cannot be detected at all (see Supporting Information Table S1).

Cl^- Effects on RuO_2; [Cl^-] = 0.3 M. Drastically different behavior is observed in 0.3 M Cl^- containing solution as shown in Figure 2d. The O_2 signal cannot be used as a normalization standard because the O_2 evolution is clearly suppressed by the presence of Cl^- and thus the DEMS data cannot be used for

quantitative comparisons. The increase of the ethene consumption (i_{26}) by more than 1 order of magnitude, however, indicates that the ethene oxidation is greatly enhanced (Figures 2d and 3). The data for i_{44} and i_{26} from Figure 2d are plotted as a function of potential in Figure 3. The peak in the i_{44} signal observed in lower Cl^- concentrations during the sweep to more positive potentials (Figure 2b and c) is now near the edge of the DEMS detection limit. Increase of the $\Delta q_{26}/\Delta q_{44}$ ratio to 40 suggests that the CO_2 reaction channel of the ethene oxidation (Table 2) is greatly suppressed. In addition, a notable change of the abundance for fragments with m/z of 15, 29, 31, 43, and 70 can be observed. While the fragment with m/z of 70 represents gaseous Cl_2 evolved at the electrode, the remaining fragments can be tracked to organic products of ethene oxidation. The time dependence of the DEMS signals i_{26}, i_{15}, and i_{29} during three consecutive potential sweep cycles on RuO_2-900 electrode is shown in Figure 4. The rest of the monitored fragment abundances recorded during the same experiment can be found in Supporting Information Figure S4. The fragments with m/z of 15 and 29 can be attributed to two conceivable ethene oxidation products, acetaldehyde or oxirane (see Table 1). The ratio of the integral intensities (see Figure 4) of both fragments ($\Delta q_{29}/\Delta q_{15}$ ~1.2) favors the assignment of both DEMS signals to oxirane ($\Delta q_{29}/\Delta q_{15}$ = 1.15) formation rather than to acetaldehyde ($\Delta q_{29}/\Delta q_{15}$ = 2). The clear increase of i_{31} can be, in the given context, attributed to 2-chloroethanol accumulating in the system (Supporting Information Figure S4). Further comparison of the integral intensities of the monitored fragments reveals that both the i_{44} and i_{43} integral intensities (Δq_{44} and Δq_{43}) are attributed to oxirane and Δq_{43} also to a small part to 2-chloroethanol. Therefore, the CO_2 forming reaction pathway is effectively closed at high Cl^- concentrations on the RuO_2-900 electrode. Also, the value of Δq_{43} confirms the assignment of Δq_{15} and Δq_{29} to oxirane since it is too low to match acetaldehyde.

Table 2. DEMS Integral Intensity Ratios in 0.1 M $HClO_4$, 0.3 M NaCl[a]

$\Delta q_{m/z}/\Delta q_{m/z}$	RuO_2-400	RuO_2-900	$Ru_{0.8}Co_{0.2}O_2$
$\Delta q_{26}/\Delta q_{15}$	54	50	75
$\Delta q_{26}/\Delta q_{31}$	47	23	17
$\Delta q_{26}/\Delta q_{43}$	142	158	135
$\Delta q_{26}/\Delta q_{44}$	40	42	18
$\Delta q_{15}/\Delta q_{31}$	0.9	0.5	0.3
$\Delta q_{32}/\Delta q_{70}$	2.7	0.6	0.2

[a] Integral intensities for corresponding fragments were obtained by integration of DEMS signals as illustrated in Figure 4 and Supporting Information Figure S1.

Electrocatalyst Effects; [Cl^-] = 0.3 M. To get more insight into the role of Cl_2 and O_2 evolution in the process, the ethene oxidation in 0.3 M NaCl was investigated on the other two electrode materials considered in this study. As expected, the selectivity of the studied materials toward O_2 and Cl_2 evolution follows the same trend in ethene-saturated solution as without ethene (see Supporting Information Figure S5).[22,24] The O_2/Cl_2 formation selectivity ratio gradually decreases from the lowest for RuO_2-400 to the highest for $Ru_{0.8}Co_{0.2}O_2$. This can be described by the $\Delta q_{32}/\Delta q_{70}$ ratios listed in Table 2. The analysis of fragment abundances with m/z of 15 and 29 during electrode polarization, already described for RuO_2-900, was also carried out for RuO_2-400 and $Ru_{0.8}Co_{0.2}O_2$. No qualitative difference was found in the DEMS analysis results (see Supporting Information Figures S6 and S7) as well as in the $\Delta q_{29}/\Delta q_{15}$ ratios and oxirane was also identified as the ethene oxidation product. The potential dependence of the ethene consumption (m/z = 26) and oxirane production (m/z = 15) measured on RuO_2-400 is shown in Figure 5a. Corresponding onsets of the electrode current and O_2 and Cl_2 DEMS signals are indicated in the upper

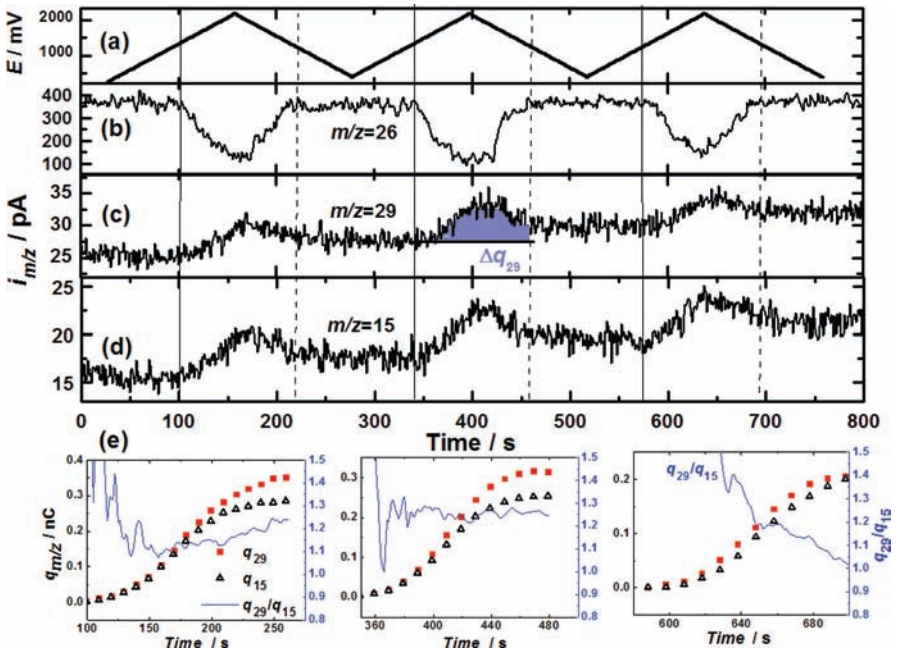

Figure 4. Mass spectrometer response as a function of time during electrode polarization according to (a) the potential ramp, sweep rate = 15 mV s^{-1}, $i_{m/z}$ with (b) m/z = 15, (c) m/z = 29, and (d) m/z = 26 in 0.1 M $HClO_4$, 0.3 M NaCl saturated with ethene. (e) Calculated integral intensities for m/z of 15 and 29 and the $\Delta q_{15}/\Delta q_{29}$ ratio. The vertical lines are added to guide the eye and to highlight the integration intervals.

dx.doi.org/10.1021/ja109955w | J. Am. Chem. Soc. 2011, 133, 5882–5892

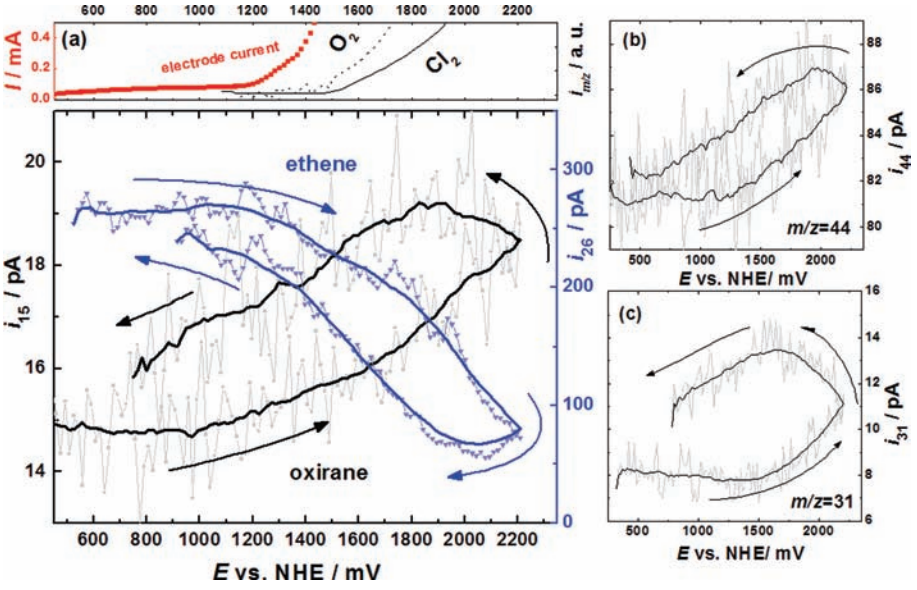

Figure 5. Mass spectrometer signals $i_{m/z}$ for (a) m/z = 15 and m/z = 26, (b) m/z = 44, and (c) m/z = 31 in relationship with potential measured on RuO_2-400 electrode in 0.1 M $HClO_4$, 0.3 M NaCl saturated with ethene. Simultaneously measured current and mass detection of O_2 and Cl_2 are depicted in the top part of panel a. The thick lines obtained by smoothing (adjacent averaging, 15 points) are shown to guide the eye. Sweep rate = 15 mV s^{-1}.

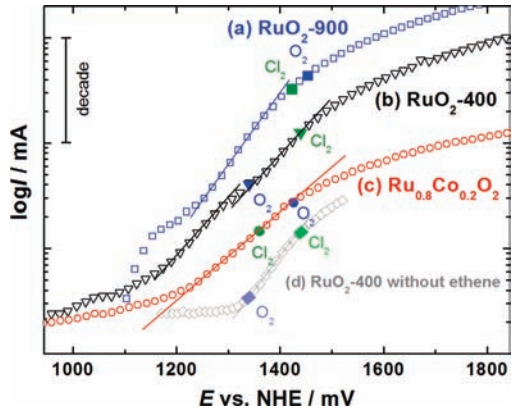

Figure 6. Logarithmic dependence of electrode current on potential recorded on the (a) RuO_2-400, (b) RuO_2-900, and (c) $Ru_{0.8}Co_{0.2}O_2$ electrodes in 0.1 M $HClO_4$, 0.3 M NaCl saturated with ethene and in (d) ethene-free solution on RuO_2-400. The lines are added to guide the eye. The actual currents measured on different electrodes are similar and were shifted with respect to vertical axes to show all the data in one figure. The onset potentials for O_2 (blue) and Cl_2 (green) evolution as measured by DEMS in the ethene-free solutions are marked on the polarization curves for each electrode.

part of Figure 5a. Simultaneously recorded i_{44} and i_{31} signals can be found in Figure 5b and c, respectively. The potential interval of the oxirane formation coincides with that of the ethene consumption. Unfortunately, it is impossible to precisely identify the onset potential of oxirane formation due to noisy data in Figure 5a. Logarithmic dependence of the measured current on potential in Figure 6, however, suggests that the exponential increase of the current starts below 1.2 V. This indicates a faradaic charge transfer[38] between the electrode and some oxidized species. The comparison with the current recorded at the same electrode in ethene-free electrolytes, also shown in Figure 6, suggests ethene oxidation as the only possible source of the current exponential increase. The CO_2 production is closed (Figure 5b) and 2-chloroethanol is not detected below ~1.45 V (Figure 5c). From this it follows that the oxirane formation starts below 1.2 V, which is lower than the potentials for O_2 (~1.35 V) and Cl_2 (~1.45 V) gas evolution. The same analysis was performed with the data obtained on the RuO_2-900 and $Ru_{0.8}Co_{0.2}O_2$ electrodes. The corresponding potential-DEMS signal curves can be found in the Supporting Information (Figures S8 and S9). The logarithmic dependences of the electrode current on the potential for RuO_2-900 and $Ru_{0.8}Co_{0.2}O_2$ are also shown in Figure 6. The trend observed on the RuO_2-400 electrode is general and does not depend on the actual selectivity of the catalyst toward O_2/Cl_2 evolution (Table 2). In Figure 6, onsets potentials for the O_2 and Cl_2 gas evolution are marked, as detected by DEMS in ethene-free (0.1 M $HClO_4$, 0.3 M NaCl) solution. Clear discontinuity in the logarithmic slope can be seen in the case of the RuO_2-400 electrode at the point where O_2 evolution starts. The Cl_2 evolution onset does not have such an influence in the case of the $Ru_{0.8}Co_{0.2}O_2$ material. The other gas evolution onsets appear in the potential region where the log I–E dependence is no longer linear due to mass transport contribution[38] and thus kinetics cannot be revealed in this potential region. However, the correlation between ethene oxidation and O_2 evolution observed in Figure 6 can also be illustrated by comparison of the onset potentials for O_2 and Cl_2 evolution measured in solutions with and without ethene (Figure 7). Whereas Cl^- evolution is unaffected by the presence of ethene, the O_2 evolution is suppressed and is detected at higher potentials (+~100 mV) when ethene is present. These observations indicate a link between the O_2 evolution reaction and ethene oxidation. Cl_2 evolution and ethene oxidation, on the other hand, do not seem to have any influence on each other.

An interesting feature appears in the results obtained on the $Ru_{0.8}Co_{0.2}O_2$ electrode, where a clearly pronounced peak in the

dx.doi.org/10.1021/ja109955w |J. Am. Chem. Soc. 2011, 133, 5882–5892

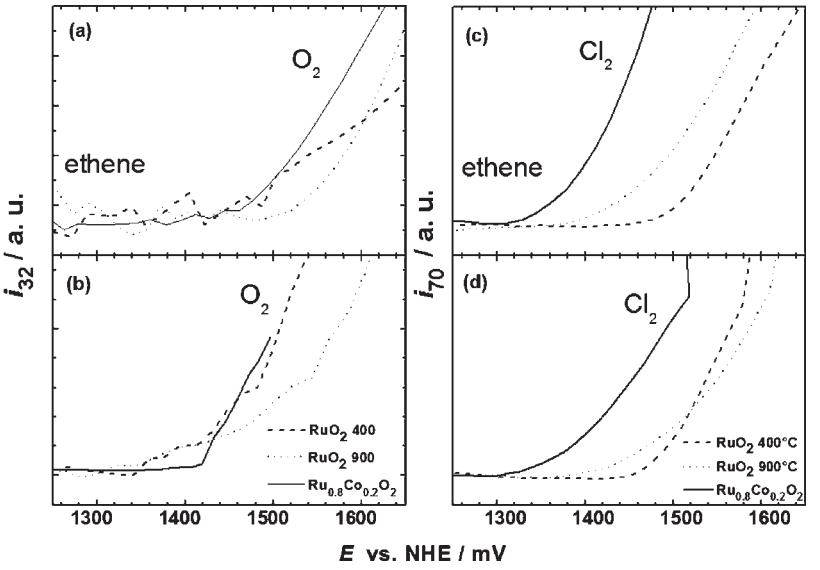

Figure 7. Online mass spectrometer detection at the gases evolution onsets for O_2 in (a) ethene-saturated and (b) ethene-free solutions and for Cl_2 in (c) ethene-saturated and (d) ethene-free solutions during polarization of electrodes composed of different materials (see figure legend) in 0.1 M $HClO_4$, 0.3 M NaCl. Sweep rate = 15 mV s^{-1}.

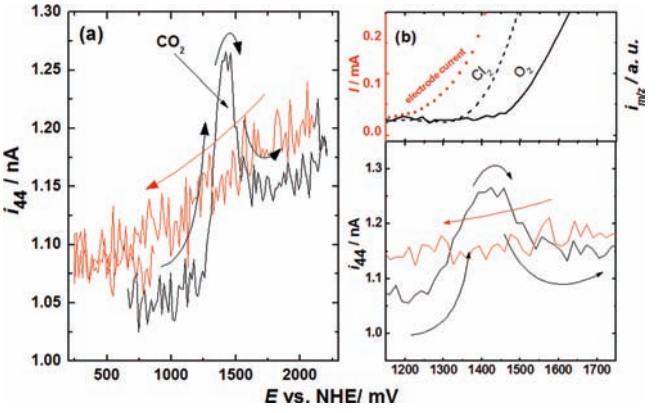

Figure 8. Mass spectrometer response for m/z = 44 as a function of potential recorded in solution containing 0.1 M $HClO_4$, 0.3 M NaCl on $Ru_{0.8}Co_{0.2}O_2$ electrode. Sweep rate = 15 mV s^{-1}.

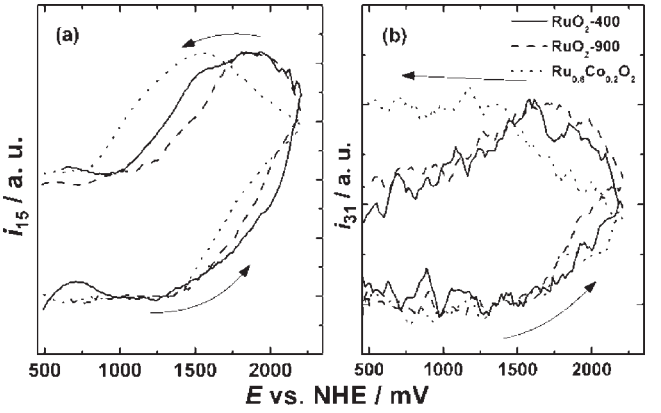

Figure 9. DEMS signals with m/z of (a) 15 and (b) 31 recorded during electrode polarization in solution containing 0.1 M $HClO_4$, 0.3 M NaCl on RuO_2-400 (solid), RuO_2-900 (dashed), and $Ru_{0.8}Co_{0.2}O_2$ (dotted) electrodes. All signals were normalized with respect to the highest intensity. The curves in panel a were obtained by smoothing of the measured data (see Figure 5). Sweep rate = 15 mV s^{-1}.

i_{44} signal was observed at 1.4 V during the positive going potential sweep, as shown in Figure 8. This peak was not observed in any other DEMS m/z channels and can therefore be attributed to CO_2 formation. The CO_2 formation, however, seems to proceed only in the potential window restricted to this peak position, and the rest of the Δq_{44} belongs to oxirane formation, as evidenced by the comparison between the Δq_{44} and Δq_{15} integral intensities. The position of the CO_2 peak coincides with the O_2 evolution onset. Similar peak is not observed on the reversed potential sweep, which indicates some irreversible changes on the surface during reactions. In the following potential sweep cycle, however, the same behavior is observed again (see Supporting Information Figure S7).

A comparison of normalized DEMS signals with i_{15} recorded during polarization of electrodes of different materials is shown in Figure 9a. The increase of the signal background indicates an accumulation of oxirane in the electrolyte as confirmed also by the background increase in the additional potential sweep cycles (see Figure 4). This is in agreement with a stability of oxirane that should slowly decompose due to hydrolysis. For hydrolysis of oxirane to yield ethane-1,2-diol was the first order rate constant at pH 1 reported to be $\sim 5 \times 10^{-5}$ s^{-1}.[39] In Cl^- presence, however, faster oxirane decay route to yield 2-chloroethanol will take place, and the first order rate constant for this reaction can be estimated of approximately $\sim 1.1 \times 10^{-3}$ s^{-1} in 0.3 NaCl at pH 1.[40] A comparison of potential dependences of i_{31}, signal attributed to formation of 2-chloroethanol, recorded on all materials is shown in Figure 9b. In the same way as in the case of oxirane (Figure 9a), an accumulation of 2-chloroethanol occurs (see Figure 9b and Supporting Information S4). The increased concentration of 2-chloroethanol in the system did not lead to the change of oxirane amount produced (Δq_{15}) in additional potential sweeps (Figure 4). This proves that 2-chloroethanol is not an intermediate for epoxide formation in the investigated system. In fact, an opposite trend should be expected as 2-chloroethanol is a

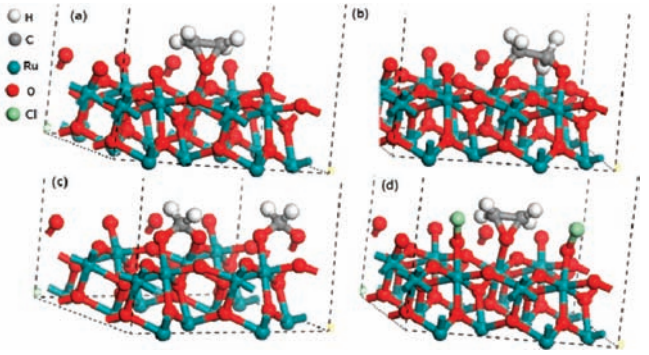

Figure 10. Two-layer RuO_2 optimized slabs with (101) crystallographic orientation and oxidized surface with possible ethene oxidation intermediates: (a) epoxide-like (Ae-1), (b) diol-like (Ad-1), (c) methylene dioxo species (Ad-2), and (d) epoxide-like with chloride ions adsorbed (AeCl-1).

product of oxirane hydrolysis in Cl^- containing acid media. In addition, the water oxidation taking place at the electrode produces protons that can accelerate the hydrolysis. Therefore, under given conditions, oxirane is likely a source of a portion of 2-chloroethanol. Again, similar integral intensity observed during additional sweeps for 2-chloroethanol (Δq_{31}) suggests that the contribution from the hydrolysis is below the equipment detection limit.

Direct comparison of the electrocatalytic activity of different electrodes is complicated by the fact that the DEMS technique has different sensitivity toward monitored reaction products. As already mentioned, sensitivity of DEMS to a particular reaction product is controlled by the product's volatility and interactions with solvent. The selectivity of different catalytic materials in ethene oxidation process, however, can be assessed by normalizing the DEMS signals of the reaction products with the signal of the ethene consumption (see Table 2). It has to be stressed that the values shown in Table 2 do not represent true conversion rates but depict the qualitative difference of the catalytic materials.[41] The data in Table 2 suggest that the oxirane production is only weakly affected by the catalyst's nature. In contrast, 2-chloroethanol production seems to track the selectivity of the catalysts toward O_2/Cl_2 evolution ($\Delta q_{32}/\Delta q_{70}$ ratio in Table 2). This is reflected in the 2-chloroethannol/oxirane ($\Delta q_{31}/\Delta q_{15}$) ratio decrease from 0.9 for RuO_2-400 to 0.3 for $Ru_{0.8}Co_{0.2}O_2$ (Table 2). The observed tendency confirms previous conclusion that the oxirane in acid media is produced in a reaction sequence independent of 2-chloroethanol formation. A comparison of the $\Delta q_{26}/\Delta q_{44}$ and $\Delta q_{26}/\Delta q_{15}$ ratios (Table 2) reveals that almost all the Δq_{44} can be connected with formed oxirane (see Table 1), which indicates that the CO_2 reaction channel is very inefficient in ethene oxidation on both RuO_2 materials in 0.3 M NaCl. An increase of CO_2 production that occurs on $Ru_{0.8}Co_{0.2}O_2$ reflects the behavior depicted in Figure 7 and discussed above. The authors would like to stress that the 50 times lower oxirane or 2-chloroethanol integral intensity with respect to that of ethene does not necessarily mean such a low conversion rate. This discrepancy is most likely only due to the above-discussed DEMS sensitivity problems as no other products of ethene oxidation were detected.

Quantum Chemical Modeling (QCM). DFT modeling was employed to understand to the role of chloride ions in the electrocatalytic process of ethene oxidation. Ethene oxidation

Scheme 1. Considered Ethene Oxidation Reaction Pathways[a]

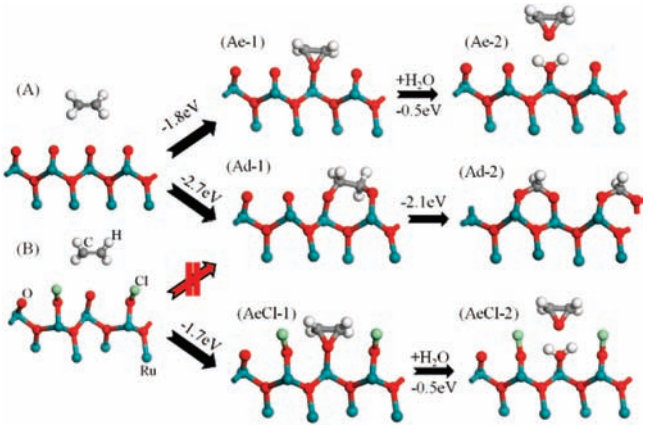

[a] Drawn structures are only illustrational and are not the actual optimized structures. Each energy step refers to the difference in stability of reactant and corresponding product (T = 0 K) as computed on the employed slabs, some of which are shown in Figure 10. The energies for isolated molecules were used in case of ethylene, oxirane, and water. Contributions of hydration of reactants and products are expected to approximately cancel.

was modeled at a RuO_2 (101) surface, which is most abundant on materials studied in the present paper. Oxygen terminated two-layer as well as three-layer slabs were considered. The oxidative conditions at the electrode at potentials $E > 1.2$ V were modeled by oxygen terminated RuO_2 (101) (Figure 10), similarly to ref 35. Two reaction pathways for ethylene oxidation were considered. One monitors the CO_2 formation channel, while the second concerns the epoxidation reaction according to the Ad and Ae pathway in Scheme 1A, respectively.

Two characteristic ethene adsorbates were considered: (1) an epoxide-like structure (Figure 10a; Scheme 1, Ae-1) where ethene binds parallel to the surface normal to a single oxygen atom and (2) the diol-like structure (Figure 10b; Scheme 1, Ad-1) where ethene again binds parallel to the surface plane forming -O-CH_2-CH_2-O- bidenate structure. Binding of ethene to a single surface oxygen (Figure 10a; Scheme 1, Ae-1) was found to be less stable by 0.9 eV relative to the bidentate structure where the ethene molecule bridges between two surface oxygen sites (Figure 10b; Scheme 1, Ad-1). Whereas the former is understood to comprise the precursor of oxirane, the latter would precede the formation of ethylenediol. For a reference, the stability of a surface methylene-dioxo compound (Figure 10c; Scheme 1, Ae-1) was determined to be 3.0 eV below the epoxide precursor (Ad-2). The methylene-dioxo species is understood to eventually lead to CO_2 evolution detected by DEMS.

The considered mechanisms according to Scheme 1 imply that the epoxide formation requires blocking of neighboring oxygen sites. Cl^- is known to be a strongly adsorbing species, suppressing the oxygen evolution.[35] Such suppression is proposed to result from competing adsorption of Cl^- at the water oxidation sites and may occur by the formation of Ru-O-Cl or Ru-Cl intermediates. Indeed, the experimentally observed behavior implies that the surface blocking has to be caused by such a stable species. In order to determine the detailed nature of the blocking species a stability of Ru-Cl and Ru-O-Cl was compared. The Ru-O-Cl decomposition reaction to form O_2 and surface

Ru-Cl was quantified by means of the above-described three-layer slabs in conjunction with the GGA PBE density functional. To avoid the problematic Kohn−Sham DFT description of $^3O_2$,[30] a two-step procedure was employed. First, the energy change is computed for the reaction:

$$2\text{Ru-OCl}_{surf} + 2H_2O(g) \rightarrow 2\text{Ru-Cl}_{surf} + 2H_2O_2(g)$$
$$\Delta H = +1.7\text{eV} \quad (1)$$

Then we take the enthalpy change for the decomposition of H_2O_2 (g) from literature:[42]

$$2H_2O_2(g) \rightarrow 2H_2O(g) + O_2(g) \quad \Delta H = -2.2\text{eV} \quad (2)$$

in order to arrive at the sought energy change for the net reaction:

$$2\text{Ru-OCl}_{surf} \rightarrow 2\text{Ru-Cl}_{surf} + O_2(g) \quad \Delta H = -0.5\text{eV} \quad (3)$$

In addition to the enthalpy change in reaction 3, the entropy change will provide a further drive forward. Hence, it is likely that surface Ru-Cl species would represent the blocked sites. Access of Cl^- to free Ru sites is possible in the oxygen evolution step where either Ru-OH or Ru-Cl may subsequently form. Already formed Ru-O-Cl surface species, however, could be kinetically stabilized and coexist on the surface. In both cases isolated Ru-O sites cause suppression of the surface diol formation, thus disabling CO_2 evolution (Figure 10d). The reaction then proceeds according to the pathway in Scheme 1B. This scenario is consistent with a resulting catalytic water consumption mechanism, maintained by surface oxygen continuously being removed and where the ethene epoxidation reaction acts as oxygen sink.

General Discussion. This paper shows that RuO_2 is an efficient catalyst for ethene oxidation in aqueous acid media. The RuO_2 electrode polarization leads to ethene oxidation to CO_2 at ~1.2 V followed by O_2 evolution as a result of water splitting at ~1.4 V (see Figure 1). The O_2 evolution reaction in the ethene presence was hindered, however, in comparison with ethene-free solutions (see Figure 7). This implies possible ethene adsorption on surface reaction sites common to both reactions. This is in agreement with the ethene oxidation pathways predicted by DFT in this paper, suggesting Ru-O surface species in the on-top (cus) position as the reaction sites (see Scheme 1). Similar suppression of O_2 evolution reaction is also observed upon an addition of Cl^-.[35] Formation of Ru-O-Cl surface species was proposed by Hansen et al., thus hindering the O_2 evolution that requires the on-top Ru-O surface sites to proceed.[35] Here, it is demonstrated that the ethene oxidation reaction is rather sensitive toward chloride concentration (see Figure 2). The increase of Cl^- concentration leads to (1) general suppression of the ethene oxidation reaction channel leading to CO_2 and (2) gradually increasing asymmetric suppression of both CO_2 production and subsequently ethene consumption at high potentials (E > ~1.6 V). Both trends may arise from the complex interplay of the adsorption phenomena on the surface where the Ru-O species in on-top position seem to govern the oxygen transfer to ethene molecule. Cl^- concentration determines the coverage of the surface by the Cl species (see QCM section) and the population of the Ru-O species will be reduced by introduction of Cl^-. The Ru-Cl species can be relatively stable and at high potentials (E > 1.3 V) removable only by reaction with Cl^- from the solution, which is inefficient at low concentrations of Cl^- ($[Cl^-] \leq 0.01$ M). The Cl occupied surface sites then act as spectators toward oxygen evolution reaction[35] and ethene oxidation toward CO_2 (see Scheme 1). In this context, the CO_2 evolution channel seems to follow the decrease of Ru-O sites population until it completely ceases. Similar reasoning can be applied to the ethene oxidation suppression at high potentials (E > ~1.6 V) where a loss of available Ru-O sites can occur due to an interference of a parallel process. Since the on-top Ru-O sites are proposed reactive sites also for the O_2 evolution reaction, competition for these sites can take place. Therefore, it is proposed here that with an increase of Cl^- concentration the system becomes more sensitive toward "Ru-O reactive site demand" and one of the competing processes could be hindered upon reaching high reaction rates. At this breaking point, the O_2 evolution proceeds very efficiently on the available surface sites, the number of which is reduced by Cl^- presence, thus causing shortage of sites for the CO_2 evolution. The proposed scenario is consistent with the theoretical results suggesting that the conversion of one ethene molecule to CO_2 requires four adjacent Ru-O sites (Scheme 1). O_2, however, needs only one[35,43] or two[21,35,43] Ru-O surface sites. The Ru-Cl surface species were also identified as efficient blocking agents in a parallel study on RuO_2 (110) in a gas phase catalysis of CO oxidation published recently.[44] The existence of such species may also explain the anticipated surface poisoning effects observed in Figure 2.

At high Cl^- concentrations (0.3 M), oxirane and 2-chloroethanol were the main reaction products of ethene oxidation while the CO_2 reaction channel was effectively shut on RuO_2. The CO_2 pathway still remains relatively efficient on $Ru_{0.8}Co_{0.2}O_2$ at low potentials but diminishes above the O_2 evolution onset during positive going potential sweep (Figure 8). This is consistent with the proposed competition between the O_2 and CO_2 evolution processes. The reason for the higher CO_2 reaction channel efficiency probably reflects a different nature of the surface oxygen sites due to Co doping. The fact that the CO_2 evolution increase is not observed during the reversed potential sweep agrees with the poisoning effects proposed above. In this context, an explanation by delayed surface blocking with, e.g., Cl occupied sites on $Ru_{0.8}Co_{0.2}O_2$ is possible. This option is consistent with the comparison of the onset potentials for O_2 and Cl_2 evolution on the studied materials. Unlike on RuO_2, Cl_2 evolution onset potential precedes that of O_2 on $Ru_{0.8}Co_{0.2}O_2$ (see Figure 6). The metal-Cl sites may not be easily formed before the O_2 evolution takes place, and thus surface blocking is not efficient on this material. Once the metal-Cl surface species form, however, the CO_2 reaction channel is closed and the surface regenerates only after reaching low potentials again (E < 1.2 V) (see Figure 8 and Supporting Information Figure S7). This scenario requires further justification and cannot be explained conclusively without detailed understanding of the Co and Ru local structure in $Ru_{0.8}Co_{0.2}O_2$, which is going to be the subject of further communications.

The amount of 2-chloroethanol relative to ethene consumption increases with materials Cl_2 selectivity (Table 2). In the case of low concentrations of Cl^- ($[Cl^-] \leq 0.01$ M), 2-chloroethanol was not detected. This suggests that the 2-chloroethanol formation depends on the amount of evolved Cl_2. Also, the 2-chloroethanol signal sets on above ~1.45 V (Figure 5), which coincides with the Cl_2 evolution onset. This points to rather homogeneous formation of 2-chloroethanol by reaction between ethene and dissolved Cl_2. A direct formation of 2-chloroethanol by an interaction with the proposed Ru-Cl or Ru-O-Cl species, however, cannot be excluded due to a high detection limit of DEMS for 2-chloroethanol. A small part of 2-chloroethanol likely

originates from acid-promoted hydrolysis of oxirane that is accelerated under proton-producing conditions at the anode.

The results of theory and experiment suggest that oxirane is formed on all considered materials by an electrocatalytic process that is independent of the O_2/Cl_2 selectivity of the electrode materials (Table 2). The sudden appearance of oxirane production in 0.3 M Cl^- above ~1.2 V is rather interesting. The DFT suggests lone surface oxygen sites (Ru-O) surrounded by Cl^- occupied spectator sites to be active in the epoxidation process. Importantly, this mechanism implies that these oxygen sites are inactive in O_2 evolution in spite of the overwhelming excess of water with respect to ethene (5.2 mM). This contributes to the discussion in the literature concerning the mechanism for the O_2 evolution, i.e., whether a single metal-ion site is sufficient for catalyzing the reaction.[45−48] Given that the proposed epoxidation mechanism is valid, these results favor the binuclear (recombination of two Ru-O sites)[21] over the mononuclear mechanism (reaction between Ru-O and H_2O from solution)[35,43] for O_2 evolution on considered surfaces, confirming conclusions of previous papers.[21,35,43]

The discovery of the electrocatalytic ethene epoxidation reported here is encouraging for further research in this rather unexplored area. Based on this finding, studies employing convection controlled techniques in the ~1.15 to ~1.45 V potential window for highly efficient epoxidation would constitute a logical step to learn more about the reaction kinetics.[38] An appealing fuel cell implementation of the findings of the present paper would be achieved by catalyst surface property modifications, replacing the anticipated Cl^- promoting effect. In this context, recent developments in syntheses of oxide materials with tailored properties[49] are promising. The onset of ethene epoxidation is found below the standard redox potential of oxygen (1.23 V), which suggests O_2 reduction as possible counter reaction in proposed fuel cell. The onset potential yet would have to be improved to meet the requirements for such fuel cell. Nevertheless, it also adds further incentive for improvement in O_2 reduction electrocatalysis with the state of the art materials working at $E <$ ~0.9 V.[50]

CONCLUSIONS

CO_2 was identified as the main ethene oxidation reaction product on nanocrystalline RuO_2 and $Ru_{0.8}Co_{0.2}O_2$ electrodes in acid media. However, gradual increase of chloride ion concentration led first to suppression and finally to effective shutting down of the CO_2 reaction channel, enabling the oxirane-forming reaction. The oxirane formation was independent of Cl_2 or O_2 evolution, and the potential for oxirane detection (~1.2 V) preceded that of O_2 and Cl_2 by ~0.2 V on RuO_2 during the sweep to more positive potentials. Within this potential window, oxirane was the only detected ethene oxidation product at RuO_2 electrodes. Besides oxirane, a portion of CO_2 was also detected in the case of $Ru_{0.8}Co_{0.2}O_2$. 2-Chloroethanol, identified as a second ethene oxidation product at higher potentials ($E >$ ~1.45 V), was formed by a process parallel to that of oxirane, mostly by a homogeneous reaction between dissolved Cl_2 and ethene. The DFT calculations performed on RuO_2 (101) showed two possibilities of ethene adsorption at the electrode surface: the less stable (by 0.9 eV) epoxide-alike structure binding toward single oxygen and the more stable diol-alike structure bridging two surface oxygen atoms. The former was identified to be the intermediate leading toward epoxide and the latter toward CO_2 formation. It is proposed that Cl acts as a surface blocking agent that hinders the possibility of the CO_2 reaction path and promotes that of oxirane. The oxirane formation then proceeds through the oxidation of ethene on Ru-O sites, which nearest neighboring Ru atoms are blocked for ethene oxidation by Ru-Cl or Ru-O-Cl surface species. Finally, ethene oxidation can serve as a probe reaction to provide insight into the complex system at hand. The proposed oxirane formation mechanism implies that the oxygen evolution reaction proceeds by binuclear (recombination) rather than by a mononuclear mechanism on RuO_2.

ASSOCIATED CONTENT

Supporting Information. Additional figures and Table S1. This material is available free of charge via the Internet at http://pubs.acs.org.

AUTHOR INFORMATION

Corresponding Author
jakub.jirkovsky@chem.gu.se

ACKNOWLEDGMENT

Financial support from the European Union project "Nanostructures for Energy and Chemicals Production" (NENA) under contract no. NMP3-CT-2004-505906 is gratefully acknowledged. Special thanks to P. Steegstra for useful discussions and to Dr. Marina V. Makarova for help with syntheses of the electrode materials.

REFERENCES

(1) Arends, I. W. C. E.; Sheldon, R. A. *Top. Catal.* **2002**, *19*, 133–141.
(2) Bellussi, G.; Carati, A.; Clerici, M. G.; Maddinelli, G.; Millini, R. *J. Catal.* **1992**, *133*, 220–230.
(3) Clerici, M. G.; Ingallina, P. *J. Catal.* **1993**, *140*, 71–83.
(4) HPPO technology; http://www.basf.com ; http://www.dow.com
(5) Zimmer, A.; Monter, D.; Reschetilowski, W. *J. Appl. Electrochem.* **2003**, *33*, 933–937.
(6) Otsuka, K.; Yamanaka, I. *Catal. Today* **1998**, *41*, 311–325.
(7) Dahms, H.; Bockris, J.O'M. *J. Electrochem. Soc.* **1964**, *111*, 728–736.
(8) Baizer, M. M. *Organic Electrochemistry*; Marcel Dekker: New York, 1973.
(9) Johnson, J. W.; Lai, S. C.; James, W. J. *Electrochim. Acta* **1970**, *15*, 1511–1518.
(10) Pastor, E.; Schmidt, V. M. *J. Electroanal. Chem.* **1995**, *383*, 175–180.
(11) Sebera, J.; Hoffmannova, H.; Krtil, P.; Samec, Z.; Zalis, S. *Catal. Today* **2010**, *158*, 29–34.
(12) Loffler, T; Baltruschat, H. *J. Electroanal. Chem.* **2003**, *554−555*, 333–344.
(13) Muller, U.; Schmiemann, U.; Dulberg, A.; Baltruschat, H. *Surf. Sci.* **1995**, *335*, 333–342.
(14) Linic, S.; Barteau, M. A. *J. Am. Chem. Soc.* **2002**, *124*, 310–317.
(15) Linic, S.; Barteau, M. A. *J. Catal.* **2003**, *214*, 200–212.
(16) Linic, S.; Barteau, M. A. *J. Am. Chem. Soc.* **2004**, *126*, 8086–8087.
(17) (a) LeDuc, J. A. M. *U.S. Patent no. 3,288,692*, 1966. (b) LeDuc, J. A. M. *Chem. Abstr.* **1967**, *66*, 43288.
(18) Torii, S.; Uneyama, K.; Ono, M.; Tazawa, H.; Matsunami, S. *Tetrahedron Lett.* **1979**, *48*, 4661–4662.

(19) Torii, S.; Uneyama, K.; Tanaka, H.; Yamanaka, T.; Yasuda, T.; Ono, M.; Kohmoto, Y. *J. Org. Chem.* **1981**, *46*, 3312–3315.
(20) Vielstich, W.; Lamm, A.; Gasteiger, H. A. *Handbook of Fuel Cells, Fundamentals, Technology and Applications*; John Wiley & Sons Ltd.: New York, 2003.
(21) Trasatti, S. *Electrochim. Acta* **2000**, *45*, 2377–2385.
(22) Jirkovsky, J.; Makarova, M. V.; Krtil, P. *J. Electrochem. Soc.* **2006**, *152*, E111–E118.
(23) Macounova, K.; Makarova, M.; Jirkovsky, J.; Franc, J.; Krtil, P. *Electrochim. Acta* **2008**, *53*, 6126–6134.
(24) Makarova, M.; Jirkovsky, J.; Klementova, M.; Jirka, I.; Macounova, K.; Krtil, P. *Electrochim. Acta* **2008**, *53*, 2656–2664.
(25) Music, S.; Popovic, S.; Maljkovic, M.; Saric, A. *Mater. Lett.* **2004**, *58*, 1431–1436.
(26) Jirkovsky, J.; Makarova, M. V.; Krtil, P. *Electrochem. Commun.* **2006**, *8*, 1417–1422.
(27) Imhof, R.; Novak, P. *J. Electrochem. Soc.* **1999**, *146*, 1702–1706.
(28) NIST Chemistry WebBook; http://webbook.nitst.gov/chemistry/
(29) (a) Delley, B. *J. Chem. Phys.* **1990**, *92*, 508–517. (b) Delley, B. *J. Chem. Phys.* **2000**, *113*, 7756–7764.
(30) Perdew, J.; Burke, K.; Ernzerhof, M. *Phys. Rev. Lett.* **1996**, *77*, 3865–3868.
(31) Delley, B. *Phys. Rev. B* **2002**, *66*, 1551251–1551259.
(32) Clark, S.; Segall, M.; Pickard, C.; Hasnip, P.; Probert, M.; Refson, K.; Payne, M. *Z. Kristallogr.* **2005**, *220*, 567–570.
(33) Vanderbilt, D. *Phys. Rev. B* **1990**, *41*, 7892–7895.
(34) *Materials Studio Release Notes, Release 5.0*; Accelrys Software Inc.: San Diego, 2009.
(35) Hansen, H. A.; Man, I. C.; Studt, F.; Pedersen, F. A.; Bligaardac, T.; Rossmeisl, J. *Phys. Chem. Chem. Phys.* **2010**, *12*, 283–290.
(36) Lundin, A.; Panas, I.; Ahlberg, E. *Phys. Chem. Chem. Phys.* **2007**, *9*, 5997–6003. Lundin, A.; Panas, I.; Ahlberg, E. *J. Phys. Chem. A* **2009**, *113*, 282–290.
(37) Lundin, A.; Panas, I.; Ahlberg, E. *J. Phys. Chem. A* **2007**, *111*, 9080–9086.
(38) Bard, A. J.; Faulkner, L. R. *Electrochemical Methods—Fundamentals and Application*; John Wiley & Sons: New York, 2001.
(39) Pritchard, J. G.; Long, F. A. *J. Am. Chem. Soc.* **1955**, *77*, 2667–2670.
(40) Bronsted, J. N.; Kilpatrick, M.; Kilpatrick, M. *J. Am. Chem. Soc.* **1929**, *51*, 428–461.
(41) More realistic conversions can be in principle calculated from DEMS data provided the effects of different volatility, polarity, and ionization cross-section of the analyzed molecules are compensated for by experimental calibration. Approximate estimate of the ability to penetrate the membrane can be addressed by boiling point comparisons (see Supporting Information).
(42) Lide, D. R. *CRC Handbook of Chemistry and Physics*, 73rd ed.; CRC Press: Boca Raton, 1993.
(43) Rossmeisl, J.; Qu, Z. W.; Zhu, H.; Kroes, G. J.; Norskov, J. K. *J. Electroanal. Chem.* **2007**, *607*, 83–89.
(44) Hofmann, J. P.; Zweidinger, S.; Seitsonen, A. P.; Farkas, A.; Knapp, M.; Balmes, O.; Lundgren, E.; Andersene J. N.; Over H. *Phys. Chem. Chem. Phys.*, in press; DOI: 10.1039/c0cp01126f.
(45) Hurst, J. K. *Coord. Chem. Rev.* **2005**, *249*, 313–328.
(46) Jurss, J. W.; Concepcion, J. C.; Norris, M. R.; Templeton, J. L.; Meyer, T. J. *Inorg. Chem.* **2010**, *49*, 3980–3982.
(47) Yang, X.; Baik, M. *J. Am. Chem. Soc.* **2008**, *130*, 16231–16240.
(48) Yang, X.; Baik, M. *J. Am. Chem. Soc.* **2006**, *128*, 7476–7485.
(49) Petrykin, V.; Macounova, K.; Shlyakhtin, O. A.; Krtil, P. *Angew. Chem., Int. Ed.* **2010**, *49*, 1–4.
(50) Stamenkovic, V. R.; Fowler, B.; Mun, B. S.; Wang, G.; Ross, P. N.; Lucas, C. A.; Markovic, N. M. *Science* **2007**, *315*, 493–497.